

The OLS–lens survey: The discovery of five new galaxy–galaxy strong lenses from the SDSS^{*}

J. P. Willis^{1†}, P. C. Hewett², S. J. Warren³, S. Dye⁴ and N. Maddox²

¹*Department of Physics and Astronomy, University of Victoria, Elliot Building, 3800 Finnerty Road, Victoria, V8V 1A1, BC, Canada*

²*Institute of Astronomy, Madingley Road, Cambridge, CB3 0HA, UK*

³*Blackett Laboratory, Imperial College of Science Technology and Medicine, Prince Consort Road, London SW7 2BW, UK*

⁴*School of Physics and Astronomy, Cardiff University, 5 The Parade, Cardiff CF24 3YB, UK*

Accepted. Received;

ABSTRACT

Bright galaxy–galaxy strong lenses are much more powerful than lensed quasars for measuring the mass profiles of galaxies, but until this year only a handful have been known. Here we present five new examples, identified via the optimal line–of–sight gravitational lens search strategy applied to luminous red galaxies in the Sloan Digital Sky Survey (SDSS). Our survey largely complements a similar survey by Bolton et al., who recently presented several new lenses. The lensed background galaxies are selected from the SDSS spectra via the presence of narrow emission line signatures, including the [OII] $\lambda\lambda 3726, 3729$, $H\beta$ and [OIII] $\lambda\lambda 4960, 5008$ lines, superposed on the spectra of the bright, intervening, deflector galaxies. Our five confirmed new systems include deflector galaxies with redshifts $z = 0.17 - 0.28$ and lensed galaxies with redshifts $z = 0.47 - 1.18$. Simulations of moderately deep (few orbits) HST–ACS imaging of systems such as these, where the lensed source is brighter than $r \sim 23$, are presented. These demonstrate the feasibility of measuring accurately the inner slope of the dark matter halo to within an uncertainty $\sigma(\gamma) \sim 0.1$, the dark matter fraction within the Einstein radius, and the mass–to–light ratio of the stars alone, independently of dynamical measurements. The high success rate of our search so far, $> 60\%$, and the relatively modest observational resources necessary to confirm the gravitational lens nature of the candidates, demonstrate that compilation of a sample of ~ 100 galaxy–galaxy lenses from the SDSS is readily achievable, opening up a rich new field in dark matter studies.

Key words: gravitational lensing – surveys – galaxies: fundamental parameters

1 THE OLS–LENS SURVEY

This is the second paper in a series presenting the discovery of new strong galaxy–galaxy lenses, i.e. systems where a background galaxy is multiply–imaged by a foreground galaxy. The motivation for this work is the opportunity such lenses give for accurately measuring the projected mass profiles in the lenses, of both the baryons and the dark matter, with greater precision than has been achieved by other methods. Analysis of galaxy–galaxy lenses requires models for the mass distribution in the lens, and the flux distribution in

the unlensed source (e.g. Wallington, Kochanek & Narayan 1996; Warren & Dye 2003; Suyu et al. 2006). The resulting model image is matched to the observed image, which provides typically hundreds of constraints because the highly stretched image extends over many resolution elements. By contrast, for lensed quasars (i.e. point sources, producing point images) the fluxes cannot be used straightforwardly, because of the possibility individual images are amplified by microlensing, leaving only the positions of just two or four images as constraints. This explains why galaxy–galaxy lenses are much more powerful than lensed quasars.

By comparison with gravitational lensing, dynamical methods typically rely on a number of assumptions, such as that the system is relaxed and is spherically symmetric. The utility of galaxy–galaxy lenses for measuring galaxy mass profiles and the advantages of lensing over dynamics are illustrated by two different analyses of the HST WFPC2

^{*} Based on observations made with the William Herschel Telescope operated on the island of La Palma by the Isaac Newton Group in the Spanish Observatorio del Roque de los Muchachos of the Instituto de Astrofísica de Canarias, and at the European Southern Observatory, Chile (programme ID: 075.A-0463).
[†] E-mail: jwillis@uvic.ca

image of the Einstein ring B0047–2808. The first, by Koopmans & Treu (2003), is principally a dynamical analysis, using the measured radial profile of the stellar velocity dispersion, supplemented by the constraint provided by the size of the Einstein ring, which measures the total enclosed projected mass. The second analysis, by Dye & Warren (2005), is a pure lensing analysis, but uses all the (flux+positional) information in the image. In both analyses the mass in the lens was assumed to comprise two components; a baryonic component with mass profile the same as the light profile, of unknown mass-to-light ratio Ψ , embedded in an elliptical non-baryonic dark-matter halo, with unknown central power-law exponent γ . The lensing analysis produced much smaller uncertainties in the parameters than the dynamical analysis (Fig. 3 in Dye & Warren, 2005).¹ The baryonic fraction of the projected mass within the Einstein radius measured in the lensing analysis is $65^{+10}_{-18}\%$ at 95% confidence. The size of the uncertainty, from a single system, is similar to that achieved by Rusin, Kochanek & Keeton (2003) in their statistical analysis of 22 lensed quasars. This further emphasises the advantage of galaxy-galaxy lenses over lensed quasars. In fact the WFPC2 image of B0047–2808 is of relatively low signal-to-noise ratio. As we show below, future observations of this and other systems with the HST-ACS High Resolution Camera (HRC), which has higher throughput and better sampling, will be substantially more powerful.

The number of galaxy-galaxy lenses known where the lensed source is reasonably bright, e.g. $r < 23$, and therefore suitable for ACS imaging, was until now very small. The situation has been transformed in the past few months, and the sample of suitable systems has increased by an order of magnitude. In the first paper in this series (Willis, Hewett & Warren 2005, hereafter WHW05) we listed the three previously known examples (Warren et al. 1996; Bolton et al. 2005; Cabanac et al. 2005) and announced the discovery of two new bright galaxy-galaxy lenses. Smith et al. (2005) have provided a further example. Our survey is based on the ‘optimal line-of-sight’ (OLS) strategy described by Hewett et al. 2000, i.e. targeting those galaxies that are most likely to lens background sources. In the current paper we present five more new bright galaxy-galaxy lenses. All seven new lenses from our survey were identified as candidates by searching for anomalous emission lines – typically [OII]3727, H β 4861 or [OIII]5007 emission – in the spectra of luminous, bulge-dominated galaxies, in the spectroscopic database of the Sloan Digital Sky Survey (SDSS). The SDSS Luminous Red Galaxy (LRG; Eisenstein et al. 2001) spectroscopic sample forms the bulk of the spectroscopic targets². Full details of our survey (hereafter the OLS-lens survey) will be provided in a future paper (Hewett et al. in preparation). A similar survey is being undertaken by Bolton et al. (2004), who list 49 candidates. The two surveys are largely complementary, and are compared and contrasted in WHW05. Immediately before submission of this paper, Bolton et al. (2006) announced the remarkable discovery of 19 new galaxy-galaxy

lenses, confirmed by their morphology in HST-ACS snapshot images. We have checked that none of our new lenses are in their list.

Our methodology for confirming spectroscopically-selected candidates is firstly to obtain deeper broadband images than the original SDSS exposures (54s on a 2.5m telescope), typically 10min exposures in the r band on a 4m telescope. Fitting of smooth model galaxy profiles is used to subtract the image of the deflector galaxy in order to search for images of the source responsible for the emission line. In the majority of cases we find either one or more images within $2''$ of the galaxy centre. But at this stage, even in good seeing conditions, $< 0.8''$, the results are usually ambiguous as to whether the system is a gravitational lens, or a chance superposition, or a peculiar galaxy core. To confirm that the system is a gravitational lens we require the spectroscopic detection of two images of the emission line on either side of the spectrum of the deflector galaxy. The r band imaging provides the information to maximise the chances of success, by aligning the slit along the line from the galaxy centre to the putative brightest lensed image. So far, following these procedures, we have confirmed seven lenses through observations of just 11 candidates. The solitary candidate that shows no evidence for lensing in an r band image of similar quality to those in Figure 2, is SDSS J212628.78+111808.0, $z_{gal} = 0.34$ and it is likely that the putative [OII] $\lambda\lambda$ 3726,3729 emission line detection at 7061 Å is spurious. Three additional candidates show evidence for the presence of extended morphologies of the background emission line source but suitable spectroscopic observations remain to be undertaken. Our success rate (and that reported by Bolton et al., 2006) demonstrates that the SDSS DR4 spectroscopic sample (Adelman-McCarthy et al., 2005) contains many tens of galaxy-galaxy lenses that are easy to identify. This resource can provide an increase in the number of confirmed galaxy-galaxy lenses by over an order of magnitude, such that the number of known galaxy-galaxy lenses could rival the number of known lensed quasars. Given the potential of galaxy-galaxy lenses to determine the mass distribution within massive galaxies, such surveys are an important development in the field of gravitational lensing.

Our final goal is to measure the mass profiles of a substantial sample of deflector galaxies through the lens inversion of deep ACS images of confirmed systems brighter than $r \sim 23$. We have undertaken end-to-end modeling of ACS observations of galaxy-galaxy lenses, in order to determine the feasibility of measuring accurate mass profiles for such a sample in a reasonable number of orbits, and to decide between the ACS-HRC and ACS Wide Field Camera (WFC, higher throughput, larger pixels; Gonzaga et al. 2005). We employ the semi-linear inversion technique of Warren and Dye (2003), and Dye and Warren (2005). An example of the modeling is shown in Fig. 1. Successive rows illustrate the input model, and the results for integrations of 1 orbit with the WFC, 1 orbit with the HRC, and 5 orbits with the HRC. The middle column shows the source (either input, or reconstructed by the inversion algorithm), and the left-column shows the image, with pixel size and noise characteristics appropriate for the selected instrument and integration time. For this simulation the integrated brightness of the lensed source was $r = 22$, the axis ratios ($q = b/a$) of the baryonic and dark matter components were $q_b = 0.69$, and

¹ Some caveats to the pure lensing analysis are noted at the end of this section.

² In practice we analyse the spectra of all SDSS galaxy sources with redshifts satisfying $z > 0.25$ for anomalous emission features. The $z > 0.25$ sample is dominated numerically by LRGs.

$q_d = 0.8$, and external shear was not modeled. The right-hand column illustrates the resulting confidence contours on the two most interesting parameters of the mass model, namely γ , the inner slope of the dark matter mass distribution, and Ψ , the restframe B–band mass–to–light ratio of the baryons. The input values of these two parameters were 0.85 and 3.0 respectively. The points to note are, firstly, that despite the lower throughput the uncertainties are smaller for the HRC than the WFC for the same integration time, as a consequence of the better sampling, and, secondly, that the uncertainties shrink approximately with the square root of the number of orbits. More quantitatively, the 95% confidence range on the inner slope are $\gamma < 1.44$ for 1 orbit with the WFC, $\gamma < 1.29$ for 1 orbit with the HRC, and $0.51 < \gamma < 1.00$ for 5 orbits with the HRC. This simulation demonstrates that for a relatively bright galaxy–galaxy lens it is feasible to measure the inner slope of the dark matter mass distribution to an accuracy $\sigma(\gamma) \sim 0.1$ with just a few orbits integration. Similarly tight constraints on Ψ , and on the dark matter mass fraction inside the Einstein radius are obtained.

The above analysis rests on a number of simplifying assumptions, including that the central dark-matter density profile is of power-law form, that the dark-matter isodensity contours have constant ellipticity, that external shear is negligible, and that a constant M/L for the baryons is appropriate. Relaxing any of these assumptions could introduce strong correlations between parameters, and so increase the uncertainties. Fortunately the new HST-ACS data (e.g. Bolton et al., 2006) are of much higher S/N than the system analysed by Dye and Warren (2005), and will allow more elaborate mass models to be explored. It is worth emphasising that the analysis of galaxy-galaxy lenses is in its infancy, and deep images of a large number of systems will allow exploration of the relative value, in providing constraints on the mass profile, of different image configurations (due to the variables of source impact parameter, lens ellipticity, and source size, which determines the ring thickness).

In the next section we describe the follow-up imaging (§2.1) and spectroscopic (§2.2) observations of the five new lenses, and then discuss the evidence that each of the systems is a gravitational lens. In §3 we provide a brief summary.

2 FOLLOW-UP IMAGING AND LONG-SLIT SPECTROSCOPY OF THE CANDIDATE SAMPLE

In the following discussion all quoted r and i magnitudes refer to the SDSS filter set, and are on the AB system.

2.1 Imaging

Deeper red-band observations of the five lens systems presented in this paper were performed during two separate observing runs. Table 1 provides details of the imaging observations of the five new systems. Successive columns list the object name, the J2000 coordinates, the telescope+camera combination, the seeing, the filter, and the integration time. The systems J1246+0440 and J1446-0248 were imaged in

non-photometric conditions using the Prime Focus Imaging Camera (PFIP (*sic*)), with the Harris red filter, hereafter R , at the 4m William Herschel Telescope (WHT) on 2005 May 16 and 13 respectively. The systems J1150+1016, J2156+1204 and J2231-0849 were observed with the European Southern Observatory (ESO) Multi-Mode Instrument (EMMI), with the Gunn red filter, hereafter r_G , at the 3.5m ESO New Technology Telescope (NTT) during 2005 June 6–7, in clear conditions. The data were processed employing standard CCD reduction techniques. For both filters R and r_G we computed the photometric zero point, and colour term to convert to r using the SDSS measured r and i magnitudes of stars in each frame. Then, using the SDSS measured $r - i$ colour of each target galaxy, we calibrated the counts in the galaxy to the r system. Note that photometric conditions are not required for calibration performed in this way.

To look for evidence of lensing (arcs or multiple images), the surface brightness distribution of the deflector galaxy was modeled and subtracted. We used the elliptical Sersic model for the surface-brightness profile, convolved with the point spread function, defined by stars in the frame. The model has the following seven free parameters: x , y , orientation, ellipticity, half-light radius $r_{0.5}$, surface brightness $\Sigma_{0.5}$ at $r_{0.5}$, and Sersic index n . The fitting was iterated, successively improving the masking of any underlying images revealed. Fuller details of the fitting procedure are provided in Wayth et al. (2005). While the subtraction in each case is visually satisfactory and therefore suitable for the purposes of searching for lensed images, in most cases the χ^2 of the fit is formally unsatisfactory. Table 2 provides the best-fit values of the three parameters $r_{0.5}$, $\Sigma_{0.5}$, and n for each system, together with the computed total magnitude. The remaining entries in Table 2 are the total magnitude of the source image (see below), the source redshift (from §2.2), and the redshift and velocity dispersion (if provided) of the lens galaxy, taken from the SDSS database.

We find very good agreement between our lens–galaxy total magnitudes and the SDSS de Vaucouleurs–model total magnitudes, in the following sense. For values of $n > 4$ our total magnitudes are brighter than the SDSS model magnitudes, as would be expected, because at large radii, beyond the fitted region, our surface brightness profiles fall off less steeply than the de Vaucouleurs model. Where our measured profiles have $n < 4$ the opposite is true. Plotting the magnitude difference between our model and the SDSS model against n , and fitting a linear relation, the offset at the value $n = 4$ is only 0.04mag.

The images of the five fields both before and after subtraction are displayed in Fig. 2. Each image is oriented to match the position angle of the spectroscopic observation such that the slit lies horizontally in these images. In each case, subtraction of the galaxy surface brightness profile revealed the presence of additional sources within 1–2'' of the galaxy centroid, i.e. within the typical Einstein radius expected if the galaxy is acting as a massive deflector³. We note that the residual image features displayed in Fig. 2

³ For example, for a singular isothermal sphere at $z = 0.4$, of one-dimensional velocity dispersion $\sigma_v = 220 \text{ km s}^{-1}$, the angular diameter of the Einstein ring is 1''.5 and 2''.2 for source redshifts of $z = 1$ and $z = 4$ respectively.

Figure 1. Application of the semi-linear method to simulated Einstein ring images. The top row shows the input source surface brightness distribution (centre) and the noiseless, unsmearred lensed image (left). The lens model comprises a baryonic Sersic profile with mass to light $\Psi = 3$ and a generalised NFW dark halo with slope $\gamma = 0.85$. Successive rows show, from left to right; 1) The simulated ring image, particular to the ACS camera and number of orbits as labeled, 2) The reconstructed source, 3) The 68%, 95%, 99% and 99.9% marginalised confidence limits on the best-fit lens parameters Ψ and γ . The dot in each of the right hand panels indicates the input parameter values of the simulated deflector.

Table 1. Details of the imaging observations of the five systems

Lens	RA	Dec.	Telescope+Camera	Seeing	Filter	Exposure time (s)
J1150+1016	11 50 17.016	+10 16 52.94	NTT/EMMI	1.3''	r_G	3 × 300
J1246+0440	12 46 45.610	+04 40 25.00	WHT/PFIP	1.1''	R	3 × 300
J1446-0248	14 46 02.630	-02 48 27.88	WHT/PFIP	0.8''	R	2 × 300
J2156+1204	21 56 27.149	+12 04 11.69	NTT/EMMI	0.8''	r_G	2 × 300
J2231-0849	22 31 08.018	-08 49 25.50	NTT/EMMI	0.7''	r_G	3 × 300

are, in some cases, not unlike features anticipated from the subtraction of an imperfect parameterized model (i.e., to the extent that the lens galaxies are not exactly Sersic ellipsoids). However, while we acknowledge the possibility, this explanation is ruled out by the results of the long slit spectroscopy presented in §2.2. It is difficult to estimate the brightness of the sources, because they lie at small radii, where the residuals from the galaxy subtraction are greatest. Nevertheless, under the lens hypothesis, most of the flux will lie in an annulus close to the Einstein radius, whereas the worst galaxy residuals will occur at the smallest radii. With this in mind we adopted a simple recipe, integrating the flux in the subtracted frames in an annulus of radial extent $0.75'' < r < 2.00''$. These values are entered in Table 2. We have not attempted to estimate the uncertainty on these values, which are dominated by systematic errors associated with the galaxy subtraction. The average estimated source total magnitude is $r = 22.1$, which is encouraging in the light of the simulations presented in Fig. 1.

We now discuss each image in turn.,

J1150+1016: The subtracted image shows a promising incomplete-ring structure like a horseshoe. At the same time there are relatively large +/- residuals near the galaxy centre, and we found that the flux distribution around the candidate ring was somewhat sensitive to the exact masking of the source employed. This is as expected given the rather poor seeing (Table 1) and the relative faintness of the source (Table 2). Therefore while we might expect a higher-resolution image of the system to present a somewhat different morphology, the image is nevertheless very suggestive of lensing, and we oriented the slit E-W to maximise the chance of detecting the emission line on either side of the lensing galaxy.

J1246+0440: The subtraction reveals a pair of faint images either side of the galaxy centre, consistent with the lensing hypothesis. The flux ratio between the two residual images was rather sensitive to the exact mask used. The positive residuals are substantially larger than the negative residuals. Therefore we were confident that both images are real, and aligned the slit to include both.

J1446-0248: We see two relatively bright residual images, either side of the target galaxy, consistent with the lensing hypothesis. We aligned the slit to include both images.

J2156+1204: This image is rather complicated. There is an elongated image, resembling an inclined spiral at $3''$ to the S, and a smaller image $1''$ further to the S. In our spectrum we detect continuum from the latter, and an emission line near 7233\AA from the former. The line might be [OII] $\lambda\lambda 3726, 3729$ or $H\alpha$ $\lambda 6565$, but in either case the object is not at the redshift of the target galaxy or of the source. The measured source magnitude quoted in Table 2 will be brighter than the reality because some flux from this object will be included in the measurement annulus. Closer in, a faint residual structure reminiscent of the horseshoe seen for J1150+1016 is weakly visible. Similar remarks about the morphology of the structure apply here i.e. it is suggestive of lensing, but a higher-resolution image may look somewhat different. We aligned the slit NS, as the image indicates flux from the source on either side of the target galaxy along this axis.

J2231-0849: The residual image for this source shows a remarkably bright ring. Varying the region masked made little difference to this conclusion, and we considered it highly likely that this is a bright example of an Einstein ring. We aligned the slit to intersect the brightest part of the ring.

2.2 Spectroscopy

We followed the same procedures for the spectroscopy as in WHW05, i.e. we oriented the slit at a position angle suggested by the imaging, and then after data reduction and sky subtraction, we subtracted the spectrum of the deflector galaxy, and searched for paired images of an emission line on either side of the position of the galaxy, at the wavelength of the emission line(s) detected in the original SDSS spectrum. Finally we extracted near-optimal spectra of the sources to search for additional lines to corroborate the redshifts. Only brief details of the procedures for subtracting the galaxy spectrum, and extracting the source spectrum are provided here. The reader is referred to WHW05 for fuller details.

Spectroscopic observations were performed during 2005 June 6–7 using the Red Image Low Dispersion (RILD) configuration of the EMMI instrument at the ESO NTT. Systems J1150+1016, J1446-0248, J2156+1204 and J2231-0849 were observed using EMMI Grism #6 and a $1''$ slit, providing spectral coverage from 5800 to 8500\AA , at a resolv-

Figure 2. Follow-up r_C/R -band images for each lens system (see Table 1 for details). For each system the left and right panels show the image before and after subtraction of the deflector galaxy surface brightness profile (see text). The centroid of the galaxy surface brightness distribution is indicated in each unsubtracted frame by a white cross. In each case the centroid of the subtracted galaxy image is located between the residual images. The orientation of the image of each system has been selected to match the corresponding two-dimensional spectral image of each system displayed in Fig. 3. The exact slit/image rotation angles for each system are shown in Table 3.

Table 2. Measured properties of the deflector and source galaxies in each system

	J1150+1016	J1246+0440	J1446–0248	J2156+1204	J2231–0849
$r_{0.5}$ (arcsec)	2.02 ± 0.05	1.70 ± 0.04	3.67 ± 0.11	4.88 ± 0.51	1.57 ± 0.01
$\Sigma_{0.5}$ (r mag/arcsec ²)	22.68 ± 0.05	21.97 ± 0.05	23.90 ± 0.06	24.91 ± 0.22	21.67 ± 0.02
n	5.08 ± 0.11	5.36 ± 0.12	5.66 ± 0.11	7.71 ± 0.36	3.00 ± 0.03
lens r	17.64	17.27	17.51	17.73	17.45
source r	22.8	23.9	21.9	22.3	19.7
z_s	0.801	0.465	0.697	1.176	0.597
[OII] λ 3727 flux ($\times 10^{-17}$ ergs s ⁻¹ cm ⁻²)	54 ± 6	52 ± 6	26 ± 4	46 ± 5	89 ± 8
z_l	0.284	0.169	0.206	0.257	0.175
σ_v (kms ⁻¹)	...	217 ± 19

ing power ~ 1500 . System J1246+0440 was observed with EMMI Grism #5 and a 1'' slit, providing spectral coverage from 4000 to 7000Å, at a resolving power ~ 1100 . The spatial scale at each configuration was 0''.33 pix⁻¹. Integrations were typically split into either three or four exposures of 1800s each. The slit position angle and exposure time used for each system are provided in Table 3. The typical atmospheric seeing over the two observing nights was 0''.8 to 1''.0 although observations of J1246 were performed in 1''.2 seeing. Conventional procedures were followed for bias subtraction and flatfielding. The multiple frames for each target were then averaged, employing a sigma-clipping algorithm in order to remove cosmic ray events.

Small sections of the final frames for each system are shown in Fig. 3. For each system, the upper panel shows the reduced two dimensional frame prior to sky subtraction. After sky subtraction, a low order cubic spline function was fit up each column. This is effective in subtracting the spectrum of the lens galaxy (at wavelengths away from the strongest absorption lines). The resulting frames, convolved with a Gaussian of $\sigma = 1$ pixel, for display purposes only, are provided in the lower panels for each system. All analysis was undertaken on the unconvolved frames. All systems show an emission line at the expected wavelength, split on either side of the lens galaxy. In each case we conclude that the emission line seen is [OII] $\lambda\lambda$ 3726,3729, and consequently the detected object lies at a redshift larger than the target galaxy. These two facts combined are sufficient to conclude that each system is a gravitational lens. We note that two dimensional long slit spectroscopy provides only limited constraints on the detailed image morphology of the lensed emission line source. The important point however, is that resolution of the emission line source into multiple components provides compelling evidence for the lensing hypothesis. We discuss each system in turn below.

In Table 3 we summarise the characteristics of the image configuration, as measured in the spectrum, for each system, listing the image splitting, the impact parameters of the primary (A, i.e. brightest) and secondary (B) images, the flux

ratio, and the signal-to-noise ratio (SNR) of the detection of the fainter image. In some cases the SNR of the detections of the two images is less than in the r -band images. Nevertheless, because the contrast of the line over the spectrum of the galaxy is much greater than in the r -band images, the systematic errors from subtraction of the galaxy will be smaller. Therefore we consider that the relevant quantities summarised in Table 3 are more reliably derived from the spectroscopic frames than from the r -band images.

We extracted one dimensional spectra of the deflector galaxy and the bright and faint images of the lensed emission-line galaxy in each system using the procedure described in WHW05. The procedure models each component (deflector galaxy plus images A and B) on the reduced two-dimensional spectral frame as a Gaussian spatial profile of specified Full-Width at Half-Maximum (FWHM). The relative spatial separation of the components and the flux ratio between image A and B are fixed. The fitting procedure computes a best-fitting system centroid and vertical normalisation for the deflector galaxy and image A component by minimising the χ^2 statistic. The resultant two-dimensional model provides the relative contribution of the deflector galaxy, image and A and B at each spatial pixel, permitting straightforward extraction of the data for each source. The extracted spectra of the sources are plotted in Fig. 4.

We now discuss each system in turn:

J1150+1016: The emission line is clearly resolved into multiple spatial components. The evidence that the line is [OII] $\lambda\lambda$ 3726,3729 is the observation that the lines are double peaked at a separation corresponding to the [OII] doublet. The absence of other emission lines in the spectrum corroborates this identification but the definitive evidence comes from the detection of very strong [OIII] $\lambda\lambda$ 4960,5008 emission in the original SDSS spectrum. The measured flux ratio for this system is at first sight peculiar. For a simple model of a singular isothermal sphere (SIS) and a point source, for images A and B at impact parameters a and b , one predicts a flux ratio $a/b = 0.61 \pm 0.20$, inconsistent

Table 3. Details of the spectroscopic observations of each system, and the measured parameters for the detected [OII] $\lambda\lambda 3726, 3729$ lines. The designation image “A” is assigned to the brightest of the two source images measured in emission line flux. The measured image separations are affected by systematic uncertainties associated with the subtraction of the galaxy spectrum. We use a nominal uncertainty of $0''.1$.

	J1150+1016	J1246+0440	J1446-0248	J2156+1204	J2231-0849
Slit position angle ($^\circ$ EofN)	90	-10	100	0	135
Exposure time (s)	3×1800	3×1800	4×1800	3×1800	4×1200
Image separation ($''$)	2.62	1.83	1.73	2.12	2.16
Galaxy - A ($''$)	1.00	1.23	1.12	1.06	1.36
Galaxy - B ($''$)	1.63	0.60	0.64	1.06	0.80
Flux ratio A/B	1.92	2.83	3.60	1.12	1.11
SNR(B)	19.5	15.8	5.0	10.3	20.3

Figure 3. Two-dimensional reduced spectroscopic frames of each lens system. For each system, the upper and lower panels correspond to different stages of the analysis. In each case, the spectral axis is oriented vertically (with lower wavelengths at the bottom of the panel) and the spatial axis is oriented horizontally: the displayed dimension of each panel is approximately $24'' \times 60\text{\AA}$. *Upper panel:* Before sky subtraction, *lower panel:* after continuum subtraction of sources, and convolution with a Gaussian of $\sigma = 1$ pixel.

with the observed value of 1.92. However this simple rule can be completely misleading for an extended source lensed by an elliptical galaxy. The arc configuration suggested by the r -band image can be produced by an extended source straddling the astroid caustic.

J1246+0440: The emission line is clearly resolved into multiple spatial components. The emission line is not resolved (recall that this spectrum has lower resolution than the others). The evidence that the line is [OII] $\lambda\lambda 3726, 3729$ is the detection of the $H\gamma$ emission line (just blueward of a sky emission line near $\lambda 6360$), visible as the blip at the red end of the spectrum. The NTT spectrum thus directly confirms the multiple emission line detections, including $H\beta$ and [OIII] $\lambda\lambda 4960, 5008$ in the original SDSS spectrum. The r image indicates a simple two-image configuration. Therefore here the SIS model may be a reasonable approximation. The predicted flux ratio $a/b = 2.1 \pm 0.4$ is in agreement with the measured value of 2.83. From the r band image we obtain $a/b = 2.6$. The measured image separation is also consistent with the prediction of a SIS model and the SDSS deflector velocity dispersion shown in Table 2 (approximately $1''.65 \pm 0''.3$).

J1446-0248: The emission line is resolved into multiple spatial components, but the significance of the detection of the weaker image, $S/N = 5$, is the weakest of all the candidates, and the image is only visible in Fig. 3 as a faint extension to the left. The evidence that the line is [OII] $\lambda\lambda 3726, 3729$ is the observation that the lines are double peaked at a separation corresponding to the [OII] doublet, corroborated by the detection of $H\beta$ at the correct wavelength. The original SDSS spectrum also clearly shows the [OIII] $\lambda\lambda 4960, 5008$ doublet.

J2156+1204: The emission line is clearly resolved into multiple spatial components. The evidence that the line is [OII] $\lambda\lambda 3726, 3729$ is the observation that the lines are double peaked at a separation corresponding to the [OII] doublet, in agreement with the profile of the line in the original SDSS spectrum. No other emission lines are expected in either spectrum given the redshift of $z_l = 1.176$.

J2231-0849: The emission line is clearly resolved into multiple spatial components. The evidence that the line is

[OII] $\lambda\lambda 3726, 3729$ is the detection of the emission lines $H\beta$ and [OIII] $\lambda\lambda 4960, 5008$ at the correct wavelengths (Fig. 4) in agreement with the features seen in the original SDSS spectrum.

3 SUMMARY

The optimal line-of-sight selection strategy applied to the SDSS spectroscopic database provides an efficient means to identify galaxy-galaxy lenses consisting of massive bulge-dominated deflectors, $0.1 < z < 0.5$, and background lensed star-forming galaxies, $0.3 < z < 1.2$. Five new systems are presented, bringing our sample of confirmed lenses to seven. Our sample extends the upper redshift limit of the lensed galaxies from $z \simeq 0.8$ in the Bolton et al. (2006) sample to $z \simeq 1.2$. Further galaxy-galaxy lenses from very recent observing runs will be presented in a subsequent paper and many tens of high-probability candidates remain to be observed. In parallel with the work of Bolton et al. (2005, 2006) we have demonstrated the feasibility of detecting as many as 100 SDSS galaxy-galaxy lens, offering the prospect of making dramatic advances in our understanding of the mass distributions in massive galaxies. Our own simulations demonstrate that the most effective observing strategy for providing tight constraints on the inner mass profiles of individual deflector galaxies is to obtain relatively high SNR imaging of the systems with the ACS-HRC on Hubble Space Telescope.

ACKNOWLEDGEMENTS

Funding for the Sloan Digital Sky Survey (SDSS) has been provided by the Alfred P. Sloan Foundation, the Participating Institutions, the National Aeronautics and Space Administration, the National Science Foundation, the U.S. Department of Energy, the Japanese Monbukagakusho, and the Max Planck Society. The SDSS Web site is <http://www.sdss.org/>.

The SDSS is managed by the Astrophysical Research Consortium (ARC) for the Participating Institutions. The

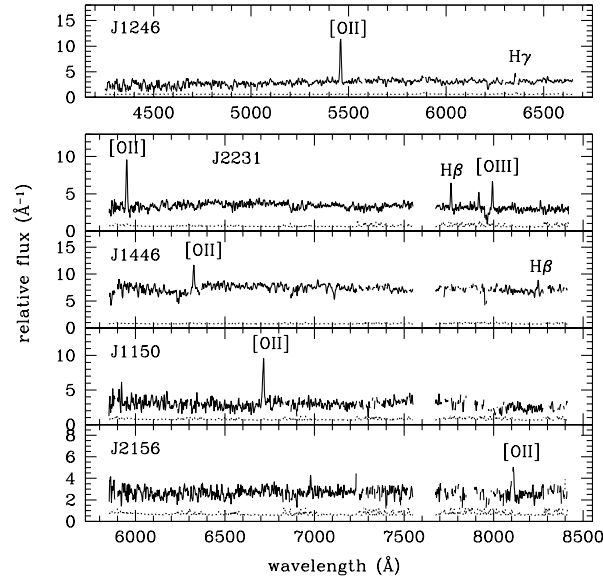


Figure 4. Extracted spectra of the source galaxies in each system. The spectra of confirmed lenses are presented in order of increasing source redshift from the top to the bottom panels. Prominent emission features are indicated. Note that J1246 was observed using a different spectrograph configuration to the other lens systems and is thus presented in a separate panel.

Participating Institutions are The University of Chicago, Fermilab, the Institute for Advanced Study, the Japan Participation Group, The Johns Hopkins University, Los Alamos National Laboratory, the Max-Planck-Institute for Astronomy (MPIA), the Max-Planck-Institute for Astrophysics (MPA), New Mexico State University, University of Pittsburgh, Princeton University, the United States Naval Observatory, and the University of Washington.

NM wishes to thank the Overseas Research Students Awards Scheme, the Cambridge Commonwealth Trust, and the Dr. John Taylor Scholarship from Corpus Christi College for their generous support.

Rusin D., Kochanek C. S., Keeton C. R., 2003, 595, 29
 Smith, R. J., Blakeslee, J. P., Lucey, J. R., Tonry, J., 2005, ApJ, 625, L103.
 Suyu S. H., Marshall P. J., Hobson M. P., Blandford R. D., 2006, MNRAS, submitted (astro-ph/0601493)
 Wallington S., Kochanek C. S., Narayan R., 1996, ApJ, 465, 64
 Warren S. J., Dye S., 2003, ApJ, 590, 673
 Willis J. P., Hewett P. C., Warren S. J., 2005, MNRAS, 363, 1369 (WHW05)

This paper has been typeset from a \TeX / \LaTeX file prepared by the author.

REFERENCES

Abazajian K., Adelman-McCarthy J. K., Agüeros M. A., et al., 2005, AJ, 129, 1755
 Adelman-McCarthy J. K., et al., 2005, AJ, in press (astro-ph/0507711)
 Bolton A. S., Burles S., Koopmans L. V. E., Treu T., Moustakas L. A., 2005, ApJ, 624, L21
 Bolton A. S., Burles S., Koopmans L. V. E., Treu T., Moustakas L. A., 2006, ApJ, 638, 703
 Bolton A. S., Burles S., Schlegel D. J., Eisenstein D. J., Brinkmann J., 2004, AJ, 127, 1860
 Cabanac R. A., Valls-Gabaud D., Jaunsen A. O., Lidman, C., Jerjen C., 2005, A&A, 436, L21
 Dye S., Warren S. J., 2005, ApJ, 623, 31
 Eisenstein, D. J., Annis, J., Gunn, J. E., et al., 2001, AJ, 122, 2267
 Gonzaga, S., et al. 2005, "ACS Instrument Handbook", Version 6.0, (Baltimore: STScI)
 Hewett P. C., Warren S. J., Willis J. P., Bland-Hawthorn J., Lewis G. F., 2000, ASPC, 195, 94
 Koopmans L. V. E., Treu T., 2003, ApJ, 583, 606

This figure "willisfig1.jpeg" is available in "jpeg" format from:

<http://arxiv.org/ps/astro-ph/0603421v1>

This figure "willisfig2.jpeg" is available in "jpeg" format from:

<http://arxiv.org/ps/astro-ph/0603421v1>

This figure "willisfig3.jpeg" is available in "jpeg" format from:

<http://arxiv.org/ps/astro-ph/0603421v1>